INTERNATIONAL JOURNAL FOR NUMERICAL METHODS IN FLUIDS, VOL. 7, 103–129 (1987)

POROUS AEROFOIL ANALYSIS USING VISCOUS–INVISCID COUPLING AT TRANSONIC SPEEDS

CHARLES R. OLLING*

Lockheed-California Co., Burbank, California 91520-7552, U.S.A.

AND

GEORGE S. DULIKRAVICH†

Department of Aerospace Engineering, Pennsylvania State University, State College, PA 16802, U.S.A.

SUMMARY

Viscous–inviscid interaction is used to compute steady two-dimensional, transonic flows for solid and porous aerofoils. A full-potential code was coupled with both a laminar/transition/turbulent integral boundary-layer/turbulent wake code and the finite-difference boundary-layer code using the semi-inverse methods of Carter and Wigton. The coupling was performed using the transpiration coupling concept, thus allowing for analysis of porous aerofoils with passive physical transpiration. The computations confirm experimental findings that passive physical transpiration can lead to a lower drag coefficient and a higher lift coefficient, a weaker shock and elimination of shock-induced separation. Nevertheless, it is very important that the extent of the porous region and permeability factor distribution of the porous region are chosen carefully if these improvements are to be achieved.

KEY WORDS Viscous–Inviscid Interaction Transonic Flows Computational Aerodynamics Surface Transpiration Flows

INTRODUCTION

Shock-free or nearly shock-free transonic configurations have favourable properties, such as minimum wave drag and no or reduced shock-induced separation.[1] Unfortunately, at off-design conditions shock-free configurations rapidly loose their advantages. In order to widen the off-design margins of almost shock-free flow one feasible approach is to modify the surface boundary conditions on the aerofoil by making a portion of the aerofoil surface porous.[2–5] Surface transpiration may be applied in an active (or forced) mode or in a passive (self-ventilated) mode. An example of a passive method is allowing the pressure inside a chamber (underneath the porous surface) to adjust to a value that is in equilibrium with Darcy's law for porous material and the external flow (Figure 1). In this case, the net mass flow through the perforated aerofoil surface is zero.

Several experimental investigations have recently been carried out for passive transpiration on an aerofoil with a perforated upper surface having a cavity underneath.

Savu *et al.*[3] made Schlieren photographs for a symmetric aerofoil with a perforated upper

*Senior Aerodynamics Engineer
†Associate Professor

0271–2091/87/020103–27$13.50
© 1987 by John Wiley & Sons, Ltd.

Received 24 January 1986
Revised 15 May 1986

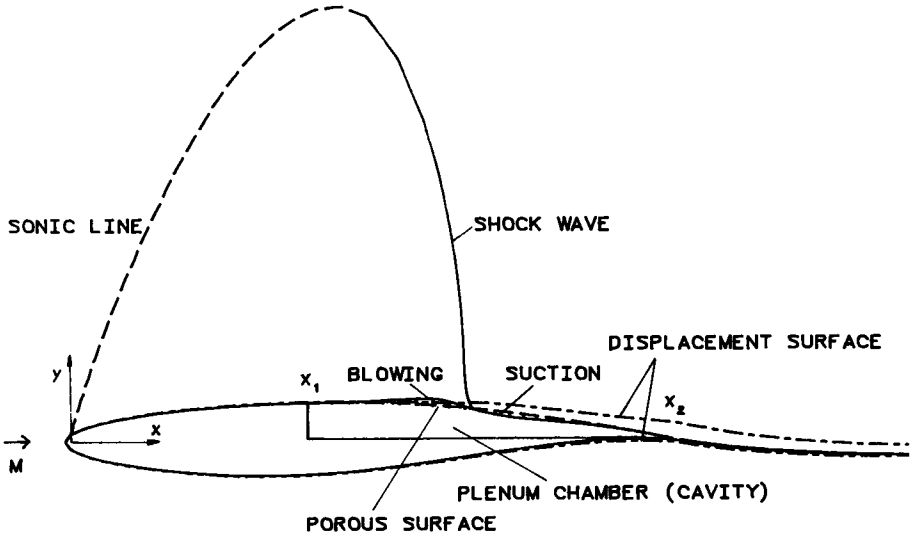

Figure 1. Passive physical transpiration for a porous RAE 2822 aerofoil

surface extending from near the leading edge to near the trailing edge. The porosity was equal to zero at the ends of the porous region and reached a single maximum inside the region. They observed that the shock wave was much weaker on the porous side of the aerofoil.

Krogmann *et al.*[5] experimentally studied a supercritical aerofoil with uniformly perforated upper surface over the length of 7·5 per cent chord. For high angle of incidence the drag coefficient was much reduced with the porous aerofoil, whereas at low incidence the drag was only slightly reduced. At $M = 0{\cdot}74$ the maximum lift coefficient was lower for the porous aerofoil than for the solid surface aerofoil. Surprisingly, at higher free stream Mach numbers the maximum lift coefficient was higher for the porous aerofoil.

Nagamatsu *et al.*[6] experimentally studied a transonic aerofoil with perforated upper surface over the length of 27 per cent chord. When the shock wave was located between the centre and rear of the porous region the drag coefficient was reduced below that for the solid aerofoil. However, slightly higher drag coefficients were found when the shock wave was forward of the centre of the porous region. No theoretical studies of viscous–inviscid interaction for porous aerofoils or cascades in the passive mode are at present available apart from the work of Olling.[7]

INTEGRAL BOUNDARY-LAYER CODE

The integral boundary layer method was chosen to be the primary means of computing the boundary layer and wake. This is because it is competitive with the finite-difference method with respect to accuracy for certain types of flow and is simpler to program and generally requires an order of magnitude less computer time[7] to run than the finite-difference method.

The boundary layer is assumed to be divided into laminar, transitional and fully turbulent regions in the streamwise direction. Near the leading edge of the aerofoil the boundary layer is assumed to be laminar. The attached laminar boundary layer is computed in the direct mode by a modified form of a compressible Thwaites method.[8] The tangential inviscid velocity on the aerofoil surface u_i is obtained from an inviscid flow solver. If laminar separation is indicated, the boundary layer is assumed to make an abrupt transition to fully turbulent flow.

Two options are available for determining transition: one option is to enforce abrupt transition at a specified point; the other option is to calculate the transition region from the empirical method

of Abu-Ghannam and Shaw[9] modified for compressibility. The start of transition is determined from an empirical correlation for the incompressible momentum thickness Reynolds number as a function of the free-stream turbulence level and an incompressible streamwise velocity gradient parameter. Other correlations are used to determine the extent of the transition region and the momentum thickness at the end of transition. Additional correlations then allow the momentum thickness, shape factor and skin friction coefficient in the transition region to be computed. Stewartson's[10] transformation is used to relate incompressible and compressible quantities. The method is invalid when the transition region includes separated flow or a shock wave or when transition extends into the wake.

The turbulent part of the boundary layer and the entire wake are calculated with the lag-entrainment integral method of Green *et al.*[11] modified by East *et al.*[12] in either the direct mode with u_i specified or in the inverse mode with the mass flux defect Q specified. Here $Q = \rho_i u_i \delta^*$ where ρ_i is the inviscid density on the aerofoil surface or wake centreline and δ^* is the boundary layer thickness. Both attached and thin separated turbulent flow can be calculated. This method is based on the solution of three ordinary differential equations: the momentum integral equation, the entrainment equation and a lag equation derived from the differential turbulent kinetic energy equation.

The original integral boundary layer equations[11] were extended to include physical surface transpiration. The extended momentum integral equation is

$$\frac{\mathrm{d}\theta}{\mathrm{d}s} = \frac{C_f}{2} - (H + 2 - M^2)\frac{\theta}{u_e}\frac{\mathrm{d}u_e}{\mathrm{d}s} + m_w, \tag{1}$$

where $m_w = (\rho_w v_w)/(\rho_e u_e)$ is the non-dimensional transpiration mass flux. Here the subscripts e and w denote the edge of the boundary layer and the wall (aerofoil surface), respectively, s is the arc length in the streamwise direction along the aerofoil or wake centreline, θ is the momentum thickness, u is the speed, C_f is the skin friction coefficient, H is the shape factor and M is the local Mach number. By considering the mass conservation for a control volume with a height extending from the aerofoil to the edge of the boundary layer δ and with a streamwise length ds, the equation for the entrainment coefficient C_E[11] is extended to

$$C_E = \frac{1}{\rho_e u_e}\frac{\mathrm{d}}{\mathrm{d}s}\int_0^\delta \rho u \,\mathrm{d}n - m_w, \tag{2}$$

where $C_E = V_E/u_e$, V_E is the entrainment velocity (positive for entrainment) and n is the co-ordinate normal to the aerofoil surface. Using the definition

$$H_1 = \frac{1}{\theta}\int_0^\delta \frac{\rho u}{\rho_e u_e}\mathrm{d}n \tag{3}$$

and combining equations (1) and (2) results in the modified entrainment equation

$$\frac{\mathrm{d}\bar{H}}{\mathrm{d}s} = \frac{\mathrm{d}\bar{H}}{\mathrm{d}H_1}\left\{C_E + m_w - H_1\left[\frac{C_f}{2} + m_w - (H+1)\frac{\theta}{u_e}\frac{\mathrm{d}u_e}{\mathrm{d}s}\right]\right\}\Big/\theta, \tag{4}$$

where $\bar{H}$ is Head's shape factor,

$$\bar{H} = \frac{1}{\theta}\int_0^\delta \frac{\rho}{\rho_e}\left(1 - \frac{u}{u_e}\right)\mathrm{d}n.$$

No change is made to the original lag equation.[11,12]

In the method of Green *et al.*[11] the skin friction coefficient C_f is computed from a correlation

depending on the value of the flat-plate skin friction coefficient C_{f0} corresponding to the momentum thickness Reynolds number Re_θ of the flow. The value of this flat-plate skin friction coefficient is modified to account for the effects to transpiration by using the relation given by Kays and Crawford (Reference13, p. 221):

$$C_{f0} = C_{f0s}\left|\frac{\ln(1+B_f)}{B_f}\right|^{1\cdot25}(1+B_f)^{0\cdot25}, \tag{5}$$

where C_{f0s} is the flat-plate skin friction coefficient for a non-porous surface and $B_f = m_w/(C_{f0}/2)$. The value of C_{f0} is determined by Newton iteration. It is assumed that the other empirical correlations used in the method of Green *et al.*[11] and modified by East *et al.*[12] are approximately the same for the case of a transpired boundary layer.

In the inverse mode the dependent variables are u_e, $\bar{H}$ and C_E. The general form[7] of the equations is

$$\frac{du_e}{ds} = -\frac{A}{B} + \frac{1}{B}\frac{dQ}{ds}, \tag{6}$$

$$\frac{d\bar{H}_e}{ds} = C + D\frac{du_e}{ds}, \tag{7}$$

$$\frac{dC_E}{ds} = E + F\frac{du_e}{ds}. \tag{8}$$

The boundary layer and wake on the upper and lower sides of the aerofoil and wake centre-line are computed separately. The skin friction coefficient is set equal to zero in the wake. The starting value for u_e is u_i. When transition is enforced the starting value for Q is determined in either of two ways. One way is to assume continuity of Q. The other way is to compute Q by assuming that it has the value that a flat-plate boundary layer would have at the same distance from the leading edge. The correction for longitudinal surface curvature suggested by Green *et al.*[11] is incorporated.

The system of equations is integrated with a fourth-order Runge–Kutta method.[14] The streamwise size is clustered toward the leading and trailing edges and is smaller than that of the inviscid code. The first derivative of the forcing function is calculated in the supersonic region by first-order accurate upstream differencing and in the subsonic region by the second-order accurate differencing using a non-uniform grid size.[14]

The coupling boundary conditions in the inviscid code on the aerofoil and wake centreline are a total transpiration velocity v_n normal to the aerofoil and jump conditions on the velocity components normal and tangent to the wake centreline. The total transpiration velocity v_n consists of two parts: an equivalent transpiration velocity v_b due to the boundary-layer displacement effect and a physical mass-weighted transpiration velocity v_c due to suction or blowing through the porous aerofoil surface, such that

$$v_n = v_b + v_c = \frac{1}{\rho_i}\frac{dQ}{ds} + \frac{\rho_w}{\rho_i}v_w. \tag{9}$$

Here ρ_w and v_w are the density and velocity of the physically transpired fluid, respectively. Along the wake centreline $v_w = 0$. It is assumed that ρ_w is equal to the adiabatic wall density

$$\rho_w = \rho_i \Big/ \left[1 + r\frac{(\gamma-1)}{2}M^2\right], \tag{10}$$

where r is the recovery factor and γ is the specific heat ratio. For laminar flow $r = (Pr)^{1/2}$

and for fully turbulent flow $r=(Pr)^{1/3}$, where Pr is the Prandtl number. For transitional flow, it is assumed that $r=(Pr)^b$ where $b=\frac{1}{2}-\gamma_{tr}/6$. Here, γ_{tr} is the intermittency factor: $\gamma_{tr}=0$ for laminar flow and $\gamma_{tr}=1$ for fully turbulent flow. Equation (9) is derived by considering the difference between the continuity equations for the inviscid and viscous parts of the flow field:[17]

$$\frac{\partial}{\partial s}(\rho_i u_i-\rho u)+\frac{\partial}{\partial n}(\rho_i v_i-\rho v)=0. \tag{11}$$

Integrating across the boundary layer results in the displacement thickness

$$\delta^*=\frac{1}{\rho_{iw}u_{iw}}\int_0^\delta(\rho_i u_i-\rho u)\,\mathrm{d}n. \tag{12}$$

The velocity jumps[17] on the wake centreline in the inviscid code are

$$\Delta v_n=\frac{1}{\rho_{iu}}\left(\frac{\mathrm{d}Q}{\mathrm{d}s}\right)_u+\frac{1}{\rho_{il}}\left(\frac{\mathrm{d}Q}{\mathrm{d}s}\right)_l, \tag{13}$$

$$\Delta u_t=-\left[K_u^*\frac{Q_u}{\rho_{iu}}(1+1/H_u)+K_l^*\frac{Q_l}{\rho_{il}}(1+1/H_l)\right]. \tag{14}$$

Here Δ indicates a jump, the subscripts u and l denote the upper and lower sides of the wake centreline, $H=\delta^*/\theta$ is the shape factor and K^* is the curvature of the displacement surface:

$$K^*=\frac{\mathrm{d}\beta}{\mathrm{d}s}, \tag{15}$$

where β is the slope of the displacement surface, approximated[15] by

$$\beta_u=\frac{\mathrm{d}y_u}{\mathrm{d}x}+\frac{\mathrm{d}\delta_u^*}{\mathrm{d}s}, \tag{16}$$

$$\beta_l=\frac{\mathrm{d}y_l}{\mathrm{d}x}-\frac{\mathrm{d}\delta_l^*}{\mathrm{d}s}. \tag{17}$$

A procedure similar to that of Collyer[16] is used to introduce the jumps in the normal and tangential velocity components into the reduced velocity potential at the points on the upper and lower sides of the wake centreline and at the fictitious points on either side of the wake centreline. The unit vector in the direction normal to the surface or wake centreline is

$$\mathbf{n}=(-y_X\mathbf{i}+x_X\mathbf{j})/\sqrt{x_X^2+y_X^2}, \tag{18}$$

where x, y are the physical cartesian co-ordinates and X is the computational co-ordinate (Figure 2). The unit tangent vector $\mathbf{t}$ is chosen to point in the downstream direction on the aerofoil and wake centreline. In Figure 2, the index $J=2$ corresponds to the aerofoil surface and wake centreline, with $I=$ IMID the leading edge, $I=$ ITS the suction side of the trailing edge, $I=$ ITP the pressure side of the trailing edge, $I=$ MAXX the upper side of the end of the wake centreline and $I=2$ the lower side of the end of the wake centreline. Then the unit vector in the tangential direction is

$$\mathbf{t}=(x_X\mathbf{i}+y_X\mathbf{j})\mathrm{IMNS}/\sqrt{(x_X^2+y_X^2)}, \tag{19}$$

where IMNS = 1 on the upper side of the aerofoil and wake centreline and IMNS = -1 on the the lower side. Since

$$u\mathbf{i}+v\mathbf{j}=u_t\mathbf{t}+v_n\mathbf{n}, \tag{20}$$

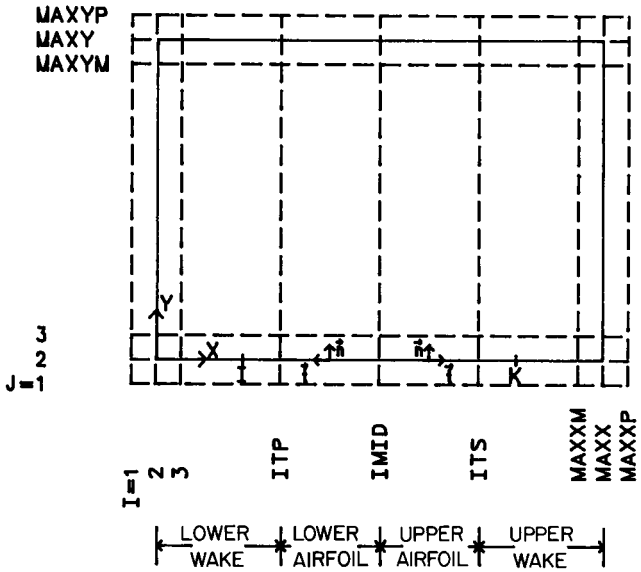

Figure 2. Computational plane with unit normal and tangent vectors on the aerofoil and wake centreline

where u, v are the Cartesian velocity components and u_t, v_n are the tangential and normal velocity components, respectively, then

$$u = (x_X u_t \mathrm{IMNS} - y_X v_n)/C_1, \tag{21}$$

$$v = (y_X u_t \mathrm{IMNS} + x_X v_n)/C_1, \tag{22}$$

where

$$C_1 = \sqrt{(x_X^2 + y_X^2)}. \tag{23}$$

Contravariant velocity vector components are defined as

$$\begin{bmatrix} U \\ V \end{bmatrix} = [J^{-1}] \begin{bmatrix} u \\ v \end{bmatrix}. \tag{24}$$

Determinant D of the geometric transformation matrix is defined as

$$D = \det[J] = \det \begin{bmatrix} x_X & x_Y \\ y_X & y_Y \end{bmatrix}. \tag{25}$$

Hence,

$$U = [u_t \mathrm{IMNS} - (x_X x_Y + y_X y_Y) v_n / D]/C_1, \tag{26}$$

$$V = C_1 v_n / D. \tag{27}$$

Next, physical velocity components can be defined as

$$u = u_\infty + G_x,$$

$$v = v_\infty + G_y, \tag{28}$$

where G is the reduced velocity potential function. Then

$$\begin{bmatrix} u \\ v \end{bmatrix} = \begin{bmatrix} u_\infty \\ v_\infty \end{bmatrix} + [J^{\mathrm{T}}]^{-1} \begin{bmatrix} \dfrac{\partial}{\partial X} \\ \dfrac{\partial}{\partial Y} \end{bmatrix} G. \tag{29}$$

Thus,

$$\begin{bmatrix} U \\ V \end{bmatrix} = [J]^{-1} \begin{bmatrix} u_\infty \\ v_\infty \end{bmatrix} + [J]^{-1}[J^{\mathrm{T}}]^{-1} \begin{bmatrix} G_X \\ G_Y \end{bmatrix}. \tag{30}$$

Solving for V in equation (30), substituting it in equation (27) and solving for v_n results in

$$v_n = D_1 G_X + D_2 G_Y + D_3, \tag{31}$$

where

$$D_1 = -(x_X x_Y + y_X y_Y)/(DC_1), \tag{32}$$

$$D_2 = C_1/D, \tag{33}$$

$$D_3 = (-y_X u_\infty + x_X v_\infty)/C_1. \tag{34}$$

From equation (21) and equation (22) it follows that

$$u_t = (x_X u + y_X v)\mathrm{IMNS}/C_1, \tag{35}$$

which after introduction of equation (29) into equation (35) gives

$$u_t = (C_3 + G_X)\mathrm{IMNS}/C_1, \tag{36}$$

where

$$C_3 = x_X u_\infty + y_X v_\infty. \tag{37}$$

On the aerofoil surface v_n is to be enforced in the inviscid flow solver. This is done by updating the reduced potential at the fictitious point at $j = 1$. Solving for G_Y in equation (31) gives

$$G_Y = (v_n - D_3 - D_1 G_X)/D_2. \tag{38}$$

Then,

$$G_{I,1} = G_{I,2} - 2(G_Y)_{I,2}. \tag{39}$$

Along the wake centreline the jumps in both u_t and v_n are to be enforced in the inviscid flow solver. During the grid generation the fictitious points overlapping the wake centreline are chosen so that x_X, y_X, x_Y and y_Y have the same magnitude but opposite signs on either side of the wake centreline, that is

$$\begin{aligned} &(x_X)_u = -(x_X)_l, \qquad (y_X)_u = -(y_X)_l, \\ &(x_Y)_u = -(x_Y)_l = 0, \quad (y_Y)_u = -(y_Y)_l. \end{aligned} \tag{40}$$

Thus,

$$\begin{aligned} &D_{1u} = D_{11} = D_1, \quad D_{2u} = D_{21} = D_2, \quad D_{3u} = -D_{31}, \\ &C_{1u} = C_{11} = C_1, \quad C_{3u} = -C_{31}. \end{aligned} \tag{41}$$

The jump in the tangential velocity component is

$$\Delta u_t = \Delta G_X / C_1, \tag{42}$$

where

$$\Delta u_t = (u_t)_u - (u_t)_l, \tag{43}$$

$$\Delta G_X = (G_X)_u + (G_X)_l. \tag{44}$$

The jump in the normal velocity component is

$$\Delta v_n = D_1 \Delta G_X + D_2 \Delta G_Y, \tag{45}$$

where

$$\Delta v_n = (v_n)_u + (v_n)_l, \tag{46}$$

$$\Delta G_Y = (G_Y)_u + (G_Y)_l. \tag{47}$$

Solving for ΔG_Y in equation (45) and using equation (42) gives

$$\Delta G_Y = (\Delta v_n - D_1 C_1 \Delta u_t)/D_2 = \sigma_1. \tag{48}$$

Solving for ΔG_X in equation (42) gives

$$\Delta G_X = C_1 \Delta u_t = \sigma_2. \tag{49}$$

Differentiating equation (49) with respect to X yields

$$\Delta G_{XX} = \frac{d}{dX}(\Delta G_X) = \sigma_3, \tag{50}$$

where

$$\sigma_3 = (x_X x_{XX} + y_X y_{XX})\Delta u_t / C_1 + C_1 \frac{d}{dX}(\Delta u_t). \tag{51}$$

Let the index K be the index for the point on the upper side of the wake centreline corresponding to the point with index I on the lower side of the wake centreline (see Figure 2). K and I are related by $I = \mathrm{MAXX} + 2 - K$. Using first-order Taylor series expansions in Y gives

$$G_{K,1} = G_{K,2} - 2(G_Y)_{K,2} + \cdots, \tag{52}$$

$$G_{K,3} = G_{K,2} + 2(G_Y)_{K,2} + \cdots, \tag{53}$$

$$G_{I,3} = G_{I,2} + 2(G_Y)_{I,2} + \cdots, \tag{54}$$

$$G_{I,1} = G_{I,2} - 2(G_Y)_{I,2} + \cdots. \tag{55}$$

Subtracting equation (54) from equation (52) gives

$$G_{K,1} = G_{I,3} + \Gamma_K - 2(\sigma_1)_I, \tag{56}$$

where Γ_K is the circulation

$$\Gamma_K = G_{K,2} - G_{I,2}. \tag{57}$$

Subtracting equation (53) from equation (55) yields

$$G_{I,1} = G_{K,3} - \Gamma_K - 2(\sigma_1)_I. \tag{58}$$

Equations (56) and (58) are used to update the reduced potential at the fictitious points on both sides of the wake centreline.

Now the reduced potential at the points on the wake centreline will be considered. From equation (49)

$$(G_{K+1,2} - G_{K-1,2}) + (G_{I+1,2} - G_{I-1,2}) = 4(\sigma_2)_I. \tag{59}$$

From equation (50)

$$(G_{K+1,2} - 2G_{K,2} + G_{K-1,2}) - (G_{I+1,2} - 2G_{I,2} + G_{I-1,2}) = 4(\sigma_3)_I. \tag{60}$$

Subtracting equation (60) from equation (59) and rearranging yields

$$\Gamma_K = \Gamma_{K-1} + 2(\sigma_2)_I - 2(\sigma_3)_I, \qquad K = \mathrm{ITS} + 1, \ldots, \mathrm{MAXX}. \tag{61}$$

where

$$\Gamma_{K-1} = G_{K-1,2} - G_{I+1,2}. \tag{62}$$

Equation (61) allows the variation of the circulation along the wake centreline to be determined. The reduced potential on the wake centreline is found from

$$G_{I,2}^{n+1} = (G_{I,2}^n + G_{K,2}^n - \Gamma_K^{n+1})/2, \tag{63}$$

$$G_{K,2}^{n+1} = G_{I,2}^{n+1} + \Gamma_K^{n+1}, \tag{64}$$

where the superscript n denotes the iteration number.

Trailing edge treatment

The expressions (42) and (45) are, in general, invalid at the trailing edge point of the aerofoil. This is because in general at that point $(y_X)_u \neq -(y_X)_l$. If the trailing edge is treated as an aerofoil point, then the proper jump of v_n will automatically be enforced by the procedure of equations (38) and (39). To enforce the required jump of u_t, the following method was applied. Let ε be a correction term to the reduced potential at the first wake centreline point such that

$$G_{\mathrm{ITS}+1,2}^{n+1} = G_{\mathrm{ITS}+1,2}^{n} + \varepsilon(1-\bar{r}), \tag{65}$$

$$G_{\mathrm{ITP}-1,2}^{n+1} = G_{\mathrm{ITP}-1,2}^{n} + \varepsilon\bar{r}k, \tag{66}$$

where $0 \leqslant \bar{r} \leqslant 1$ and $k = \pm 1$. To maintain the same average value of the reduced potential across the wake centreline set $\bar{r} = \frac{1}{2}$ and $k = -1$. The corrected reduced velocity potentials must satisfy

$$\Delta u_t = [C_{3u} + \tfrac{1}{4}(G_{\mathrm{ITS}+1,2}^{n+1} - G_{\mathrm{ITS}-1,2}^{n})]/C_{1u} + [C_{3l} + \tfrac{1}{4}(G_{\mathrm{ITP}+1,2}^{n} - G_{\mathrm{ITP}-1,2}^{n+1})]/C_{1l}. \tag{67}$$

Inserting equations (65) and (66) into equation (67) and solving for ε results in

$$\begin{aligned}\varepsilon = C_{1u}C_{1l}[&4(\Delta u_t - C_{3u}/C_{1u} - C_{3l}/C_{1l}) - (G_{\mathrm{ITS}+1,2}^{n} - G_{\mathrm{ITS}-1,2}^{n})/C_{1u} \\ &- (G_{\mathrm{ITP}+1,2}^{n} - G_{\mathrm{ITP}-1,2}^{n})/C_{1l}]/[C_{1l}(1-\bar{r}) - C_{1u}\bar{r}k].\end{aligned} \tag{68}$$

Next, the updated circulation $\Gamma_{\mathrm{ITS}+1}^{n+1}$ can be computed:

$$\Gamma_{\mathrm{ITS}+1}^{n+1} = G_{\mathrm{ITS}+1,2}^{n+1} - G_{\mathrm{ITP}-1,2}^{n+1}. \tag{69}$$

The updated circulation at the trailing edge is

$$\Gamma_{\mathrm{ITS}}^{n+1} = \Gamma_{\mathrm{ITS}+1}^{n+1} + 2(\sigma_2)_{\mathrm{ITP}-1} + 2(\sigma_3)_{\mathrm{ITP}-1}. \tag{70}$$

The reduced potential at the trailing edge is then computed from equations (63) and (64).

Pressure correction and wake curvature effect

When the jump in the tangential velocity component is enforced along the wake centreline, the inviscid pressures must be corrected to compute the viscous pressure on the wake centreline. The same correction can be applied to the aerofoil surface. The approximate method of Lock and Firmin[17] is used. The formulae for the upper and lower sides of the aerofoil and wake centreline are

$$p_{wu} = p_{iu} - K_u^* \rho_{iu} u_{iu}^2 \delta_u^* (1 + 1/H_u), \tag{71}$$

$$p_{wl} = p_{il} + K_l^* \rho_{il} u_{il}^2 \delta_l^* (1 + 1/H_l), \tag{72}$$

where p_w is the viscous pressure on the aerofoil and wake centreline and p_i is the inviscid pressure. The viscous pressure coefficient C_{pw} can be written as

$$C_{pw} = C_{pi} + C_K, \tag{73}$$

where C_K is the correction to the inviscid pressure coefficient C_{pi}:

$$C_K = \pm \frac{2}{\gamma M_\infty^2 p_\infty} K^* \rho_i u_i^2 \delta^* (1 + 1/H), \tag{74}$$

where M_∞ is the upstream Mach number, p_∞ is the upstream pressure and the plus sign corresponds to the lower side of the aerofoil or wake centreline and the minus sign corresponds to the upper side.

The viscous pressures should be the same on either side of the wake centreline. The jump in the inviscid pressure coefficient is

$$\begin{aligned}\Delta C_{pi} &= (C_{pi})_u - (C_{pi})_l \\ &= (C_K)_l - (C_K)_u. \end{aligned} \tag{75}$$

Enforcing the above jumps of the u_t and v_n in the inviscid code and then correcting the pressure as indicated does not guarantee that the viscous pressures on either side of the wake centreline will be exactly the same. This is because only the tangential velocity component is taken into account in determining C_K. When the jump of the normal velocity component is large a small jump of the viscous pressures on either side of the wake centreline will occur. The method of Van Dalsem[18] directly enforces the jump in the viscous pressures to be zero.

Contribution of transpiration velocity to the flux balance

It will now be shown how the total transpiration velocity is introduced into the mass flux balance at the aerofoil surface in the computational plane. In the computational plane the full-potential equation is

$$\frac{\partial}{\partial X}(D\rho U) + \frac{\partial}{\partial Y}(D\rho V) = 0. \tag{76}$$

During the iterative solution of the discretized from of this equation, the right-hand side is equal to a residual which is broken down into a steady part and an artificial time part. The steady part of the residual consists of the net contravariant flux out of the grid cell in the computational plane. For the aerofoil surface at $J = 2$ the cell is shown in Figure 3. The components of the contravariant flux due to the total transpiration velocity are indicated by the '0' subscript. The U and V contravariant velocity components at the centre of the cell are computed from equations (26) and (27), respectively. Since the transpiration velocity is normal to the surface, the tangential velocity component u_t in equation (26) is equal to zero. We are actually interested in the flux balance in the half cell above $J = 2$ and only extend the cell below the aerofoil surface to permit

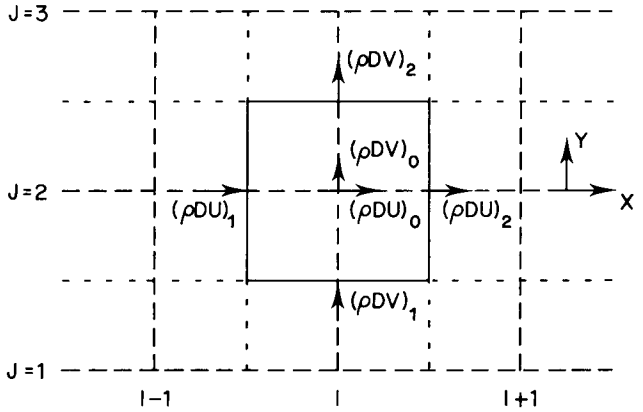

Figure 3. Mass flux computation in the computational plane at the aerofoil surface ($J = 2$)

the same second-order differencing scheme to be used on the aerofoil surface as in the interior flow field. For this upper half cell the component $(\rho DU)_0$ makes no contribution, and thus it can be excluded when considering the flux balance for the entire cell. The fluxes $(\rho DU)_1$, $(\rho DU)_2$ and $(\rho DV)_2$ can be computed from the reduced potential at the previous iteration. The flux $(\rho DV)_1$ is found by a first-order Taylor series expansion in Y:

$$(\rho DV)_2 = (\rho DV)_0 + 2\frac{\partial}{\partial Y}(\rho DV)_0, \tag{77}$$

$$(\rho DV)_1 = (\rho DV)_0 - 2\frac{\partial}{\partial Y}(\rho DV)_0. \tag{78}$$

Adding these equations and rearranging yields

$$(\rho DV)_1 = 2(\rho DV)_0 - (\rho DV)_2. \tag{79}$$

The net flux in the X-direction is

$$\text{RUDX} = (\rho DU)_2 - (\rho DU)_1 \tag{80}$$

and the net flux in the Y-direction is

$$\begin{aligned}\text{RVDY} &= (\rho DV)_2 - (\rho DV)_1 \\ &= 2[(\rho DV)_2 - (\rho DV)_0].\end{aligned} \tag{81}$$

The steady part of the residual is defined to be

$$\text{RE} = (\text{RUDX} + \text{RVDY})/D_{IJ}, \tag{82}$$

where D_{IJ} is the determinant of the Jacobian at the centre of the cell.

On the wake centreline the value of the $(\rho DV)_1$ is computed from the reduced potential, since the fictitious points in this case correspond to the physical points on the opposite side of the wake centreline.

SEMI-INVERSE COUPLING METHOD

The semi-inverse coupling method was used to couple the viscous and inviscid solutions. The formulae of Wigton[19] and Carter[20] for updating the Q values between each viscous–inviscid interaction cycle were investigated. Wigton[19] extended LeBalleur's[21] von Neumann analysis to obtain update formulae leading to a stable convergent iteration for both attached and separated transonic flow. These formulae are as follows:

For $M < 1$

$$Q^{n+1} = Q^n + \frac{\omega_1 \bar{\beta}\rho_i B u_i}{vB - \bar{\beta}\rho_i}\left(\frac{u_e}{u_i} - 1\right); \tag{83}$$

For $M > 1$

$$Q^{n+1} = Q^n + \frac{\omega_2 B\bar{\beta}\rho_i}{(Bv)^2 + (\bar{\beta}\rho_i)^2}\left[B\left(\frac{du_e}{ds} - \frac{du_i}{ds}\right) - \bar{\beta}\rho_i\left(\frac{u_e}{u_i} - 1\right)\right]; \tag{84}$$

$v = \pi/\Delta s$, Δs is the step size, $\bar{\beta} = |1 - M^2|^{1/2}$, B is the coefficient in the momentum integral equation (6) and ω_1 and ω_2 are relaxation factors (equal to unity in Wigton's analysis).

Carter's update formula is

$$Q^{n+1} = Q^n\left\{1 + \omega\left[\frac{u_e}{u_i} - 1\right]\right\}, \tag{85}$$

where ω is a relaxation factor. Wigton concluded that this formula (with $\omega = 1$) may not lead to convergent solutions for separated supersonic flow.

The semi-inverse method consists of the following steps:

1. The potential solution is advanced for a certain number of iterations on each of the increasingly refined grids with $v_n = 0$ on the aerofoil surface. Then, the boundary layer code is run in the direct mode with velocity u specified until separation or a specified point was reached. At that point the boundary layer code is switched to the inverse mode with an initial guess for Q.
2. Wigton's or Carter's formulae for updating the Q values are applied. The transpiration velocity and jumps in the velocity components along the wake centreline are computed. The potential solution is then advanced for one to five iterations on the finest grid being used, with the boundary conditions held constant. During the first few coupling cycles the relaxation factor in the inviscid flow solver was equal to unity. After that the relaxation parameter is increased to 1·7–1·8. The boundary layer code is run in the direct mode on the forward part of the aerofoil and in the inverse mode on the rest of the aerofoil and wake centreline with the Q values determined from the update formulae of Wigton or Carter.

Step 2 is repeated until the error measure $(u_e/u_i - 1)$ is less than a specified value or until a prescribed number of iteration cycles has been reached.

RESULTS

Based on the previous analytic and numerical analysis, a package of computer programs, GSD28, was developed[22] for isolated aerofoil and for cascade analysis. This software performs automatic computational grid generation, full potential finite area inviscid flow solution, integral and finite difference method solution of the complete boundary layer with wake, and automatically iteratively couples the inviscid and viscous parts of the flow field. Two examples of turbulent separating transonic flow for isolated non-lifting and lifting aerofoils were calculated.

The computer codes developed as a part of this study can also simulate the passive transpiration effects of a perforated aerofoil surface with a cavity located underneath. Darcy's law is used to determine the physical transpiration velocity[2]

$$v_w = \sigma(p_p - p_w), \tag{86}$$

$$\sigma = \bar{\sigma}/(\rho_\infty q_\infty), \tag{87}$$

where p_w is the aerofoil surface pressure, p_p is the cavity pressure (assumed to be constant), σ is the permeability factor and $\bar{\sigma}$ is the non-dimensional permeability factor: a value of $\bar{\sigma} = 0{\cdot}6$ corresponds to a geometrical porosity of about 10 per cent.[3] The plenum pressure is computed from

$$p_p = \int_s \rho\bar{\sigma}p_w \, ds \Big/ \int_s \rho\bar{\sigma} \, ds, \tag{88}$$

where s is the aerofoil surface arc length.

The physical transpiration velocity normalized by the critical speed of sound is

$$\frac{v_w}{a^*} = \frac{\bar{\sigma} M_\infty^*}{\gamma M_\infty^2} \left[\frac{\int_s \bar{\sigma} \frac{\rho}{\rho^*} \frac{p_w}{p_\infty} \frac{ds}{c}}{\int_s \bar{\sigma} \frac{\rho}{\rho^*} \frac{ds}{c}} - \frac{p_s}{p_\infty} \right], \tag{89}$$

where the asterisk denotes a critical value and p_s is the aerofoil surface pressure.

Two distributions of $\bar{\sigma}$ can be specified in the input of the present version of the code. These are a uniform distribution and a peaked distribution reaching its maximum inside the porous region and having a smooth tapering to zero at the ends of the region. The chordwise co-ordinates of the beginning (x_1) and end (x_2) of the porous region and the location of the maximum permeability (x_m) on the upper and lower sides of the aerofoil are input. The peaked distribution satisfies the following equations:

$$\bar{\sigma} = \bar{\sigma}_{max} \sin^2(\pi \bar{x}) \tag{90}$$

$$\bar{x} = [\sin(0{\cdot}5\pi x')]^b, \tag{91}$$

$$b = \ln(0{\cdot}5)/\ln[\sin(0{\cdot}5\pi x'_m)], \tag{92}$$

where

$$x' = (x - x_1)/(x_2 - x_1), \tag{93}$$

$$x'_m = (x_m - x_1)/(x_2 - x_1) \tag{94}$$

and x is the chordwise co-ordinate on the aerofoil surface.

It should be pointed out that an inviscid solution of the flow problem dealt with in this paper was recently reported by Chen *et al.*[23]

Non-lifting aerofoil example

In the first case an isolated NACA 0012 aerofoil is at zero is at zero angle of attack. This case was also considered by Wigton.[19] The upstream Mach number is 0·835 and the Reynolds number based on the chord is $24{\cdot}7 \times 10^6$. Transition was enforced at 5 per cent of the chord as in Wigton's calculations, although natural transition occurred in the actual experiment. Measurements of the pressure coefficient C_p for this test case were reported by Thibert *et al.*[24] In order to simulate the free air conditions, the gap-to-chord ratio was set equal to 16 in the input to the GSD28 computer code. The wake extended 5 chord lengths downstream. A sequence of four consecutively refined grids of C-type was used. The finest grid has 80 grid cells on both the upper and lower sides of the aerofoil, 56 cells along each side of the wake centreline and 72 C-layers of grid cells in the outward direction. The viscous boundary-layer/wake streamwise grid was more refined than the inviscid grid. The potential code was run for 150 iterations on the first grid, 100 iterations on the second grid, 80 iterations on the third grid and 5 iterations on the fourth grid. An automatic viscous–inviscid coupling was then initiated whereby one viscous boundary-layer/wake calculation was made for each additional inviscid iteration. The overrelaxation parameter in the inviscid code was 1·858 during the coupling. Carter's[20] update method was used, since it was more efficient than Wigton's update method for this case.[19] The maximum error measure ($u_e/u_i - 1$) was 0.0175 at $x/c = 0.8811$ for the solid aerofoil results shown.

The convergence rate and stability of the coupled viscous–inviscid solution could be further augmented by solving the viscous and inviscid equations simultaneously, as was demonstrated, for example, by Wai and Yoshihara[25] and more recently by Giles[26] and Drela.[27] We have attempted this approach, and the preliminary results were encouraging.[7,28]

A porous NACA0012 aerofoil simulation was performed using the peaked permeability factor

distribution on the upper and lower sides of the aerofoil with $\bar{\sigma}_{max} = 0{\cdot}10, x_1 = 0{\cdot}5$, $x_2 = 1{\cdot}0$ and $x_m = 0{\cdot}6784$.

The Mach number field is presented in Figure 4 for the solid aerofoil case and in Figure 5 for the porous aerofoil case with a converged viscous–inviscid coupled solution. The displacement surface is indicated by the dash-dot line. The pressure coefficient for the solid aerofoil is presented in Figure 6. The experimentally observed shock location is about 13 per cent of the chord length ahead of its computed location. Nevertheless, the present results predict a shock location only slightly upstream of that computed by Wigton.[19] This implies that either the experimental results are questionable or the commonly used numerical dissipation is inappropriate.[29–31] The pressure coefficient for the porous aerofoil is presented in Figure 6. The curve begins to differ from that of the solid case at the beginning of the porous region. The shock is weaker, and the shock location is moved downstream. The drag coefficient for the solid aerofoil is $C_D = 0{\cdot}04356$ (the pressure drag coefficient is $C_{D_p} = 0{\cdot}03936$ and the skin friction drag coefficient is $C_{D_f} = 0{\cdot}00421$) and that for the porous aerofoil is $C_D = 0{\cdot}04260$($C_{D_p} = 0{\cdot}03869$ and $C_{D_f} = 0{\cdot}00391$), a reduction of 2·20 per cent. The plenum pressure coefficient was $C_{pp} = -0{\cdot}4382$, and $C_p^* = -0{\cdot}3396$.

In the solid aerofoil case, the total transpiration velocity, v_n, normalized by the critical speed of sound is presented in Figure 7. In the supersonic region ahead of the shock the values are nearly constant and small. A large positive transpiration velocity occurs in the shock region and a smaller maximum occurs near the trailing edge of the aerofoil. The transpiration velocities are negative along the wake centreline.

In the porous aerofoil case, v_n starts to increase at the beginning of the porous region and the maximum in the shock region is smaller than in the solid aerofoil case. Figure 8 illustrates the

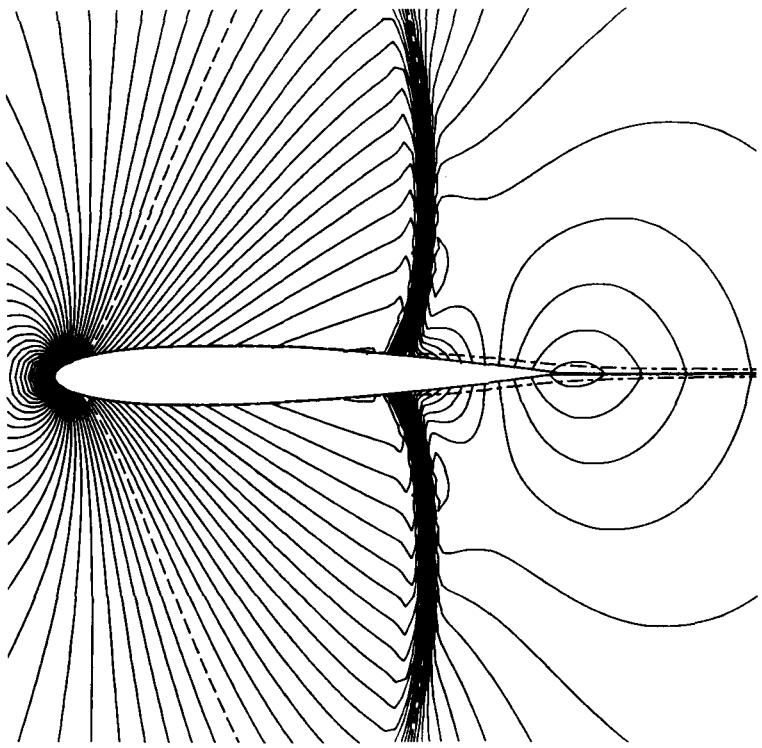

Figure 4. Mach number field with a contour interval of 0·02 near a solid NACA 0012 aerofoil

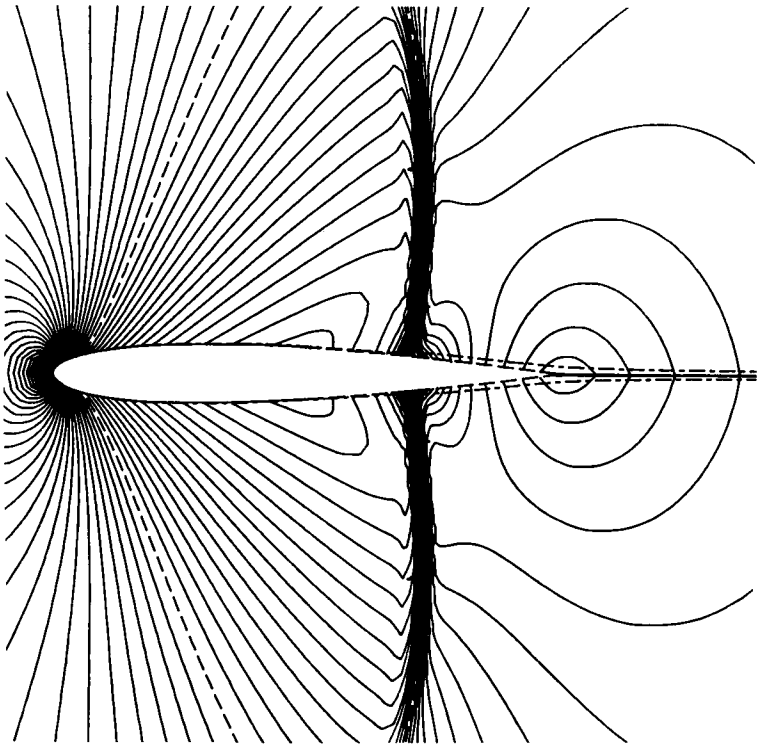

Figure 5. Mach number field with a contour interval of 0·02 near a porous NACA 0012 aerofoil

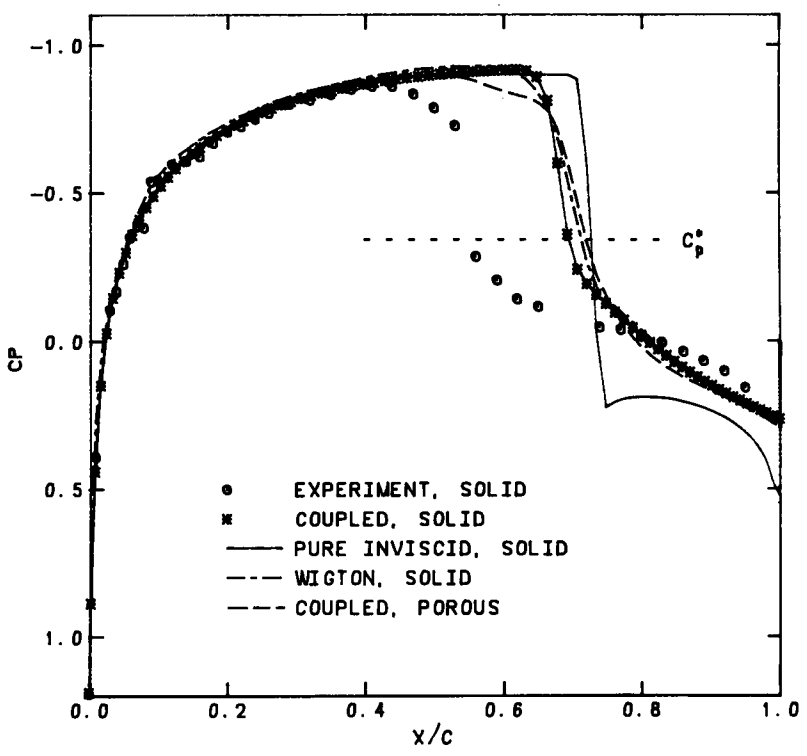

Figure 6. Pressure coefficients distribution, C_P; solid and porous NACA 0012 aerofoils

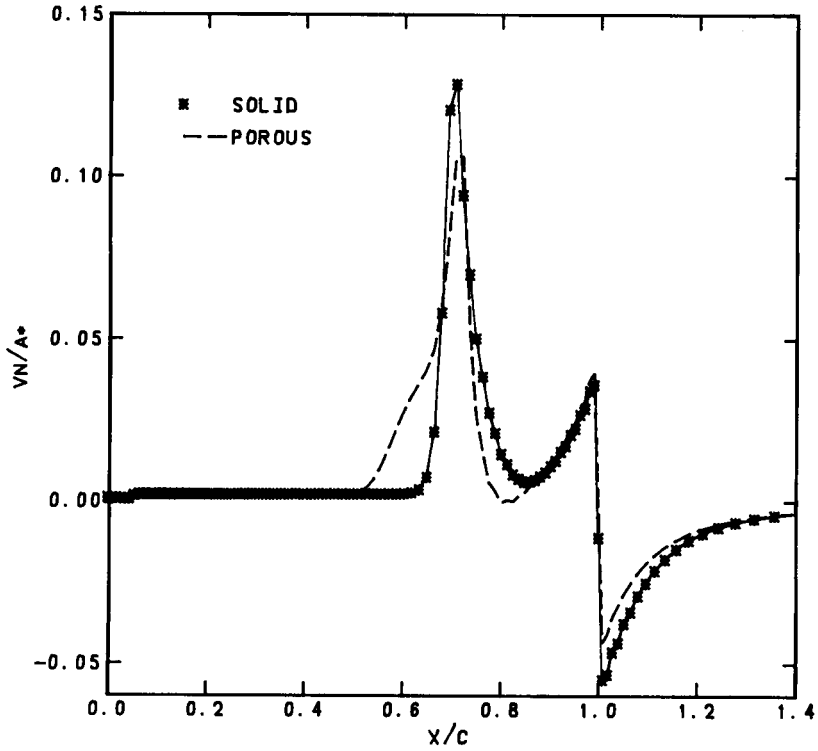

Figure 7. Total transpiration velocity, v_n/a^*; soild and porous NACA 0012 aerofoils

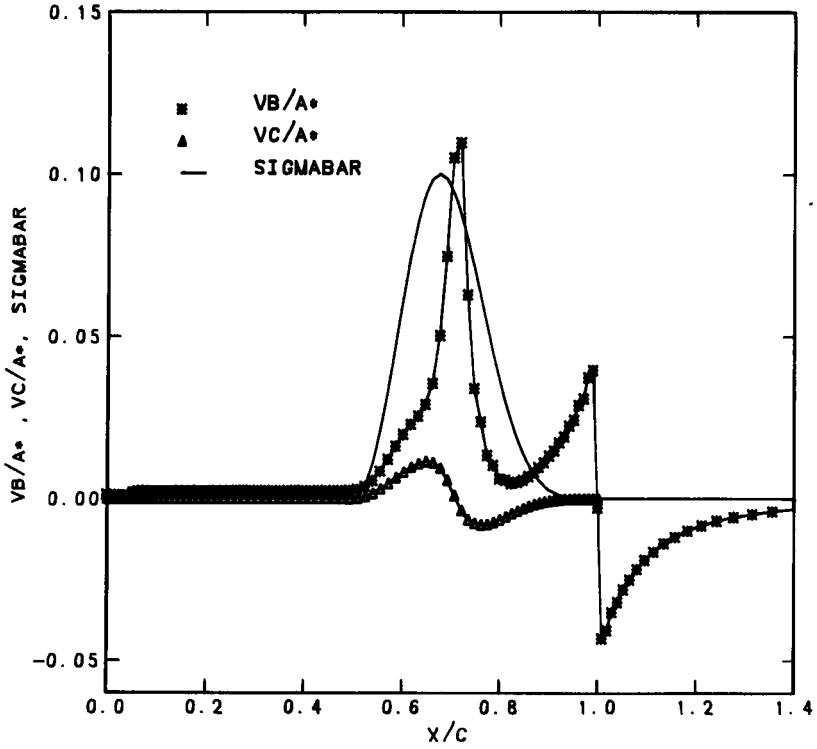

Figure 8. Equivalent and physical mass-weighted transpiration velocities, v_b/a^* and v_c/a^*, and the permeability factor $\bar{\sigma}$; porous NACA 0012 aerofoil

equivalent and physical mass-weighted transpirations velocities, v_b/a^* and v_c/a^*, and the distribution of the permeability factor $\bar{\sigma}$ for the porous aerofoil. Because the plenum C_p is close to C_p^*, physical surface blowing occurs in the supersonic region ahead of the shock and physical suction takes place behind the shock.

The displacement thickness (Figure 9) shows a rapid increase starting in the shock region slightly ahead of that of Wigton.[19] This difference may be due to the slight difference in the locations and strengths of the shocks in the two solutions obtained by the two different inviscid flow solvers. The displacement thickness near the trailing edge is reduced in the porous aerofoil case.

The skin friction coefficient (Figure 10) rapidly decreases in the laminar region and then jumps up at the enforced transition point. The calculated separated region is shifted slightly forward of Wigton's solution for the solid aerofoil. In the porous aerofoil case, the physical self-induced blowing ahead of the shock reduces C_f to near separation values, but the flow remains attached. Physical self-induced suction behind the shock leads to an increase of C_f in that region.

The momentum thickness θ/c, shape factor H and mass flux defect Q are shown in Figures 11–13 respectively.

Lifting aerofoil example

The second example is for a solid and porous RAE 2822 aerofoil. The solid aerofoil example was Case 10 of Reference 32. The free stream Mach number was 0·75. The geometric angle of attack was 3·19° and the value used in the computations was 3·033° (the same as that used by Melnik

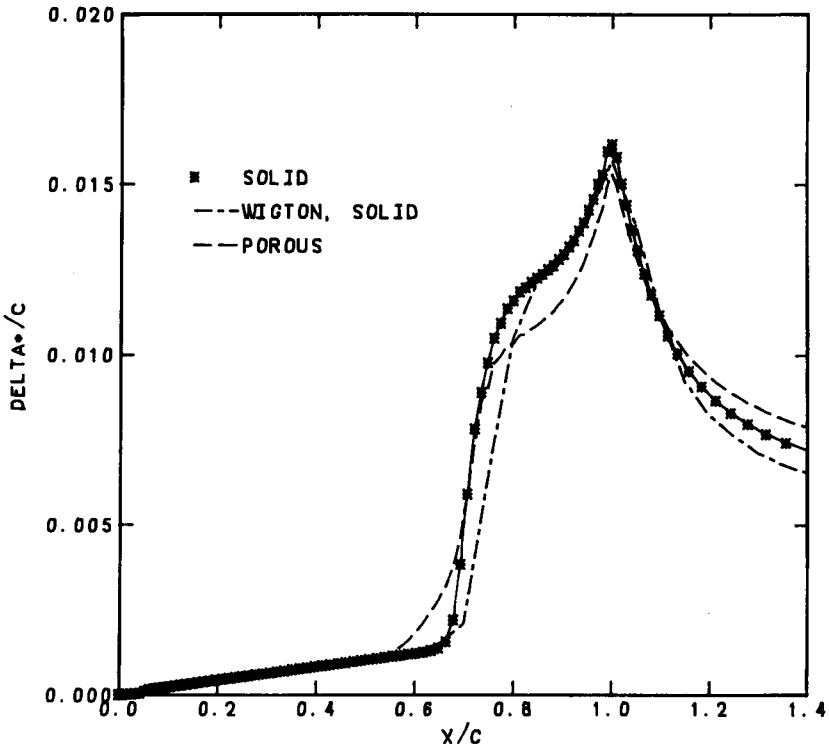

Figure 9. Displacement thickness, δ^*/c; solid and porous NACA 0012 aerofoils

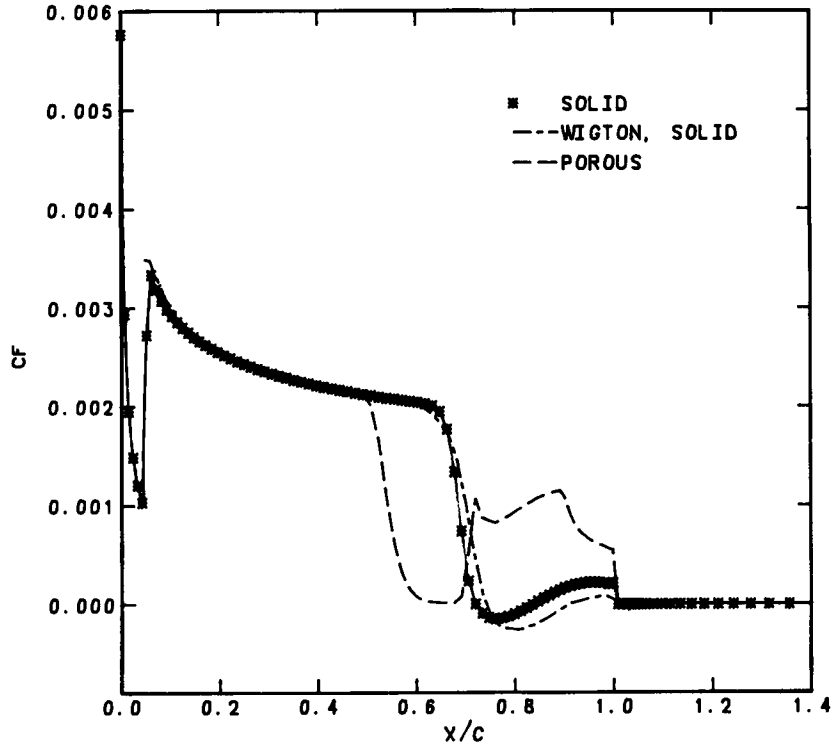

Figure 10. Skin friction coefficient, C_f; solid and porous NACA 0012 aerofoils

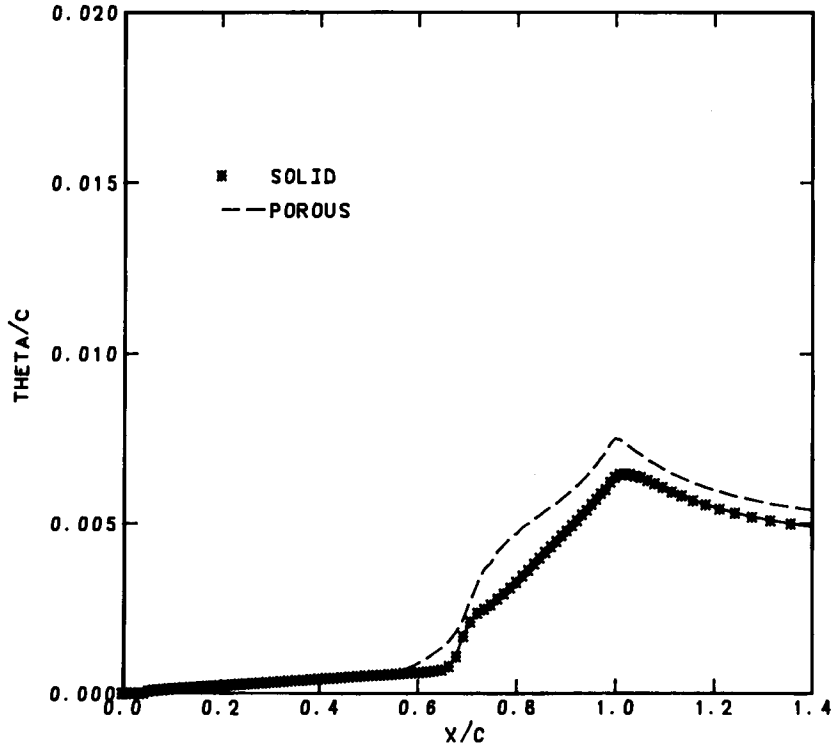

Figure 11. Momentum thickness, θ/c; solid and porous NACA 0012 aerofoils

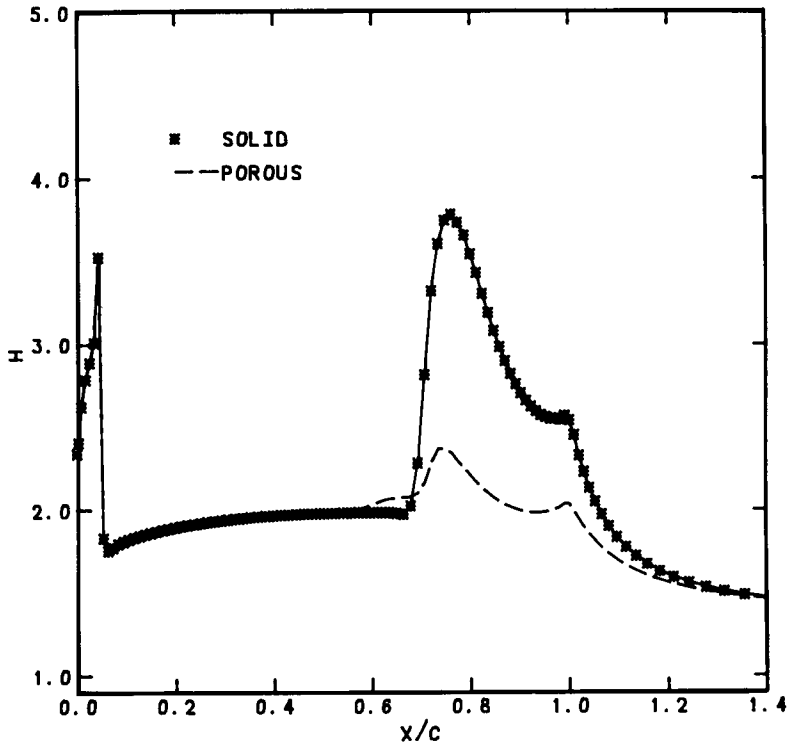

Figure 12. Shape factor, H; solid and porous NACA 0012 aerofoils

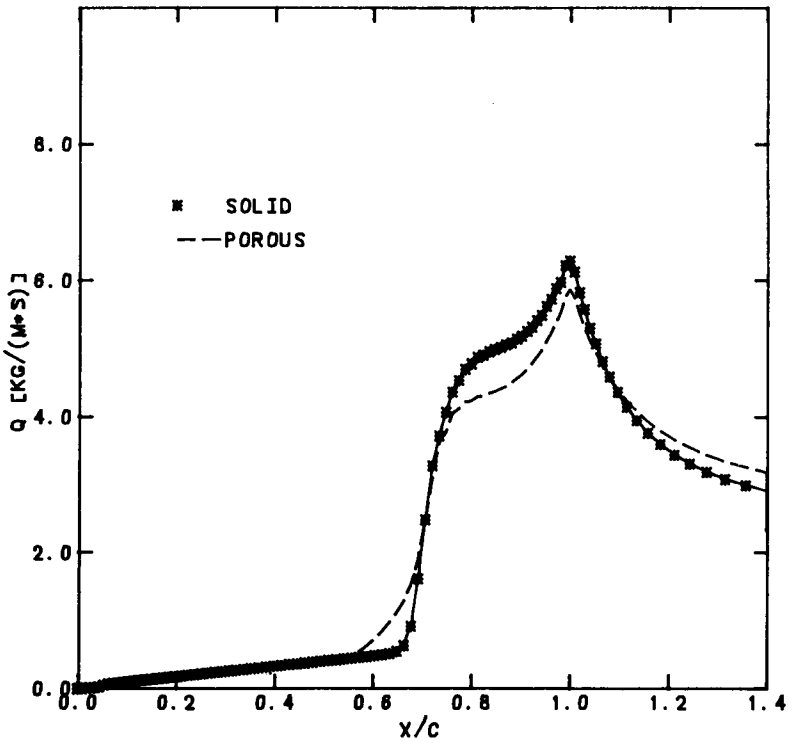

Figure 13. Mass flux defect, Q; solid and porous NACA 0012 aerofoils

et al.[33] The Reynolds number based on the chord was $6{\cdot}2 \times 10^6$. Transition was enforced at $0{\cdot}03c$.

The gap-to-chord ratio was set at 100 in the inviscid flow solver and the wake length was 30 chord lengths in order to simulate the free-air conditions more realistically. A sequence of three consecutively refined grids of C-type was used.

The porous aerofoil simulation used the peaked permeability factor distribution only on the upper side of the aerofoil, with $\bar{\sigma}_{max} = 0{\cdot}10$, $x_1 = 0{\cdot}40$, $x_2 = 1{\cdot}00$ and $x_m = 0{\cdot}6588$.

Carter's[20] update formula with a relaxation factor of 0·50 was used during the coupling. The maximum error measure $(u_e/u_v - 1)$ was 0·0314 at $x/c = 0{\cdot}8767$ on the upper side of the solid aerofoil after 400 coupling cycles.

The trailing edge treatment was used with $\bar{r} = 0$ over the last 100 coupling cycles. Its use resulted in an improved agreement between the calculated and experimental pressure coefficient distributions in the shock region.

The coupled Mach number fields near the solid and porous aerofoils for viscous–inviscid solutions are presented in Figures 14 and 15, respectively. The jump in the inviscid velocity across the wake centreline can be seen in the near-wake region.

The pressure coefficient distribution (Figure 16) shows a large difference between the coupled and pure inviscid solid aerofoil solutions, thus demonstrating the effect of a strong viscous–inviscid interaction in this case. In the porous aerofoil case, the shock is weaker and its location is moved downstream. The predicted lift coefficient for the solid aerofoil was 0·8216 and the experimental value was 0·743. The predicted lift coefficient for the porous aerofoil was 0·8379, an increase of 1·98 per cent. The predicted total drag coefficient for the solid aerofoil was 0·03032 ($C_{D_p} = 0{\cdot}02508$

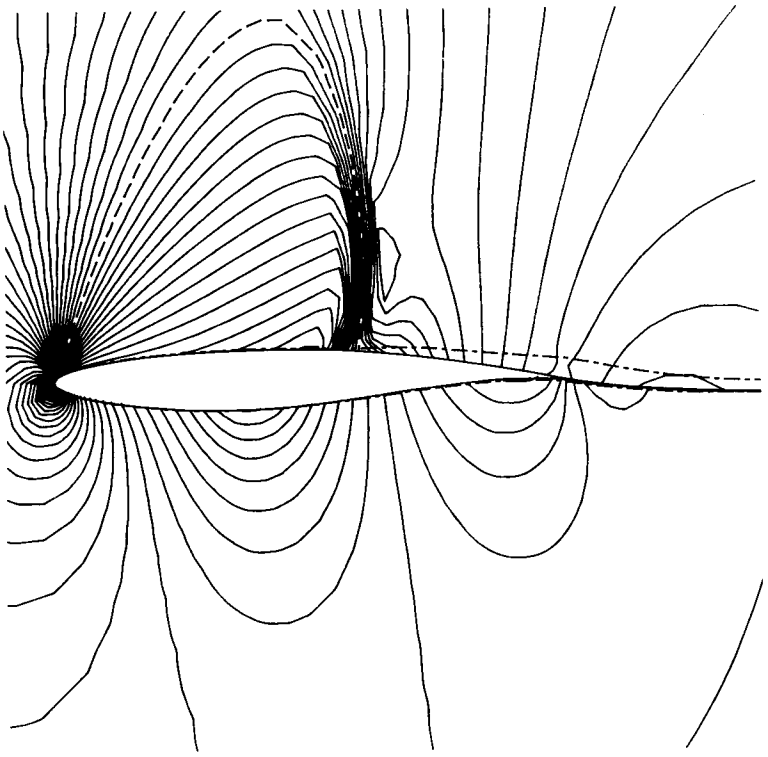

Figure 14. Mach number field with a contour interval of 0·02 near a solid RAE 2822 aerofoil

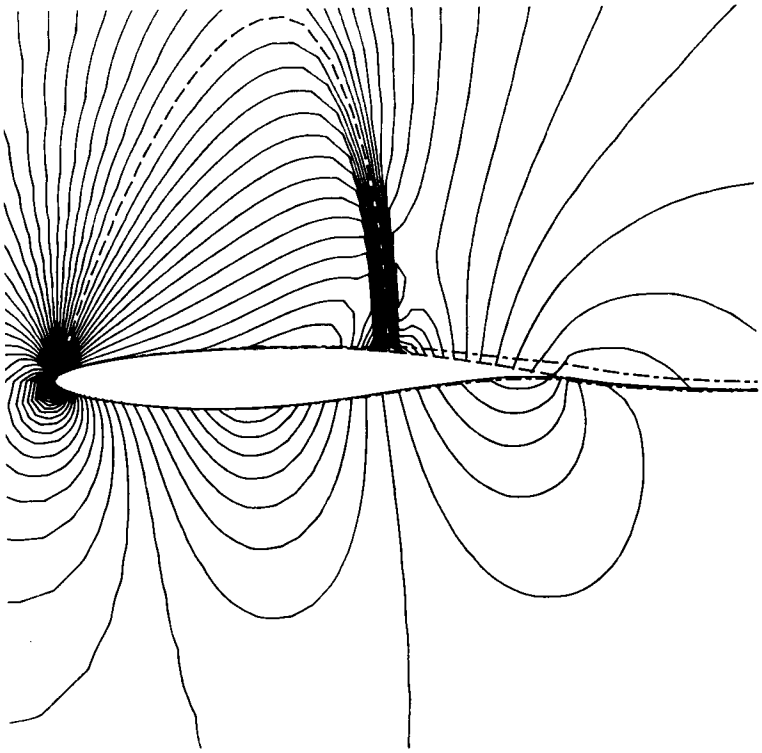

Figure 15. Mach number field with a contour interval of 0·02 near a porous RAE 2822 aerofoil

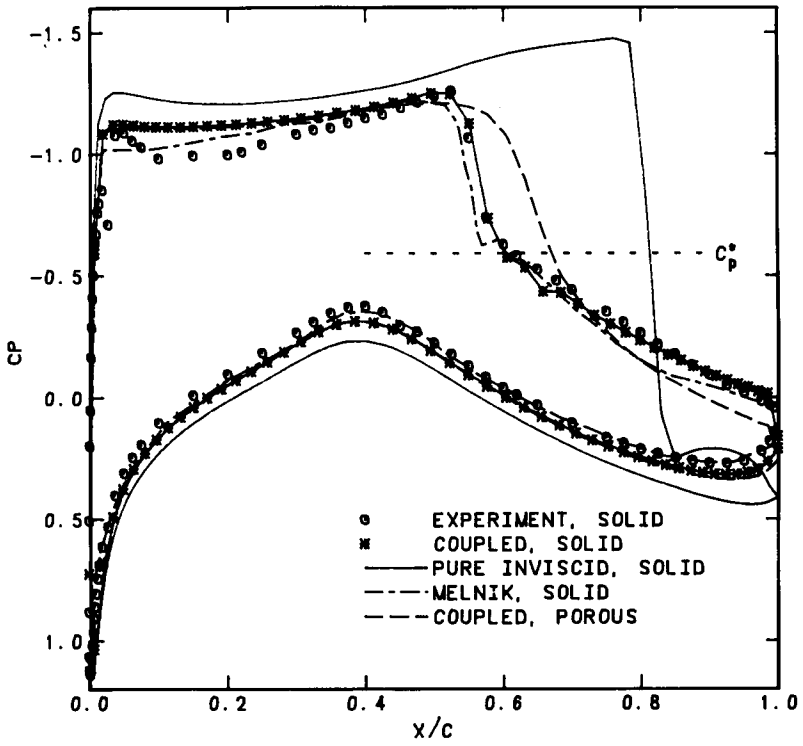

Figure 16. Pressure coefficient distribution, C_P; solid and porous RAE 2822 aerofoils

and $C_{D_f} = 0{\cdot}00524$) and the experimental value was 0·0242. The drag coefficient for the porous aerofoil was $C_D = 0{\cdot}02993$ ($C_{D_p} = 0{\cdot}02462$) and ($C_{D_f} = 0{\cdot}00531$), a decrease of 1·29 per cent. The plenum pressure coefficient was $C_{pp} = -0{\cdot}6084$, and $C_p^* = -0{\cdot}5912$.

The total transpiration velocity (Figure 17) shows high values on the upper side of the aerofoil near the shock and trailing edge. Figure 18 illustrates the equivalent and physical mass-weighted transpiration velocities, v_b/a^* and v_c/a^*, and the permeability factor $\bar{\sigma}$ for the upper side of the porous aerofoil. Because the plenum C_P is close to C_P^*, physical surface blowing occurs in the supersonic region ahead of the shock and physical suction takes place behind the shock, thus creating conditions for shock self-cancelation in the shock foot region.

The displacement thicknesses on the upper and lower sides of the aerofoil/wake centreline are shown in Figure 19. The value on the upper side near the trailing edge is overpredicted.

The skin friction coefficient on the upper and lower sides is presented in Figure 20. For the solid aerofoil case, strongly separated flow is indicated behind the shock with the separation extending to the trailing edge. Melnik's solution indicates separation somewhat earlier due to the shock being slightly forward of that in the present solution. In the porous RAE 2822 aerofoil case, separation is eliminated entirely.

The momentum thickness for the upper and lower sides is shown in Figure 21, and the shape factor is presented in Figure 22. The shape factor for the solid aerofoil near the trailing edge on the upper side does not agree well with the experimental values, owing to overprediction of the displacement thickness in that region. The mass flux defect is shown in Figure 23.

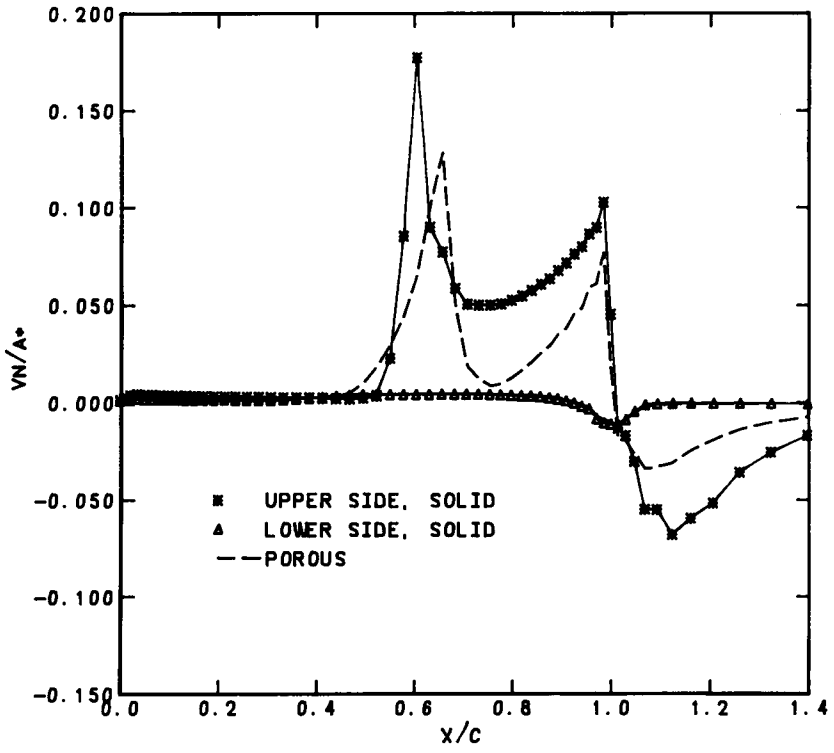

Figure 17. Total transpiration velocity, v_n/a^*; solid and porous RAE 2822 aerofoils

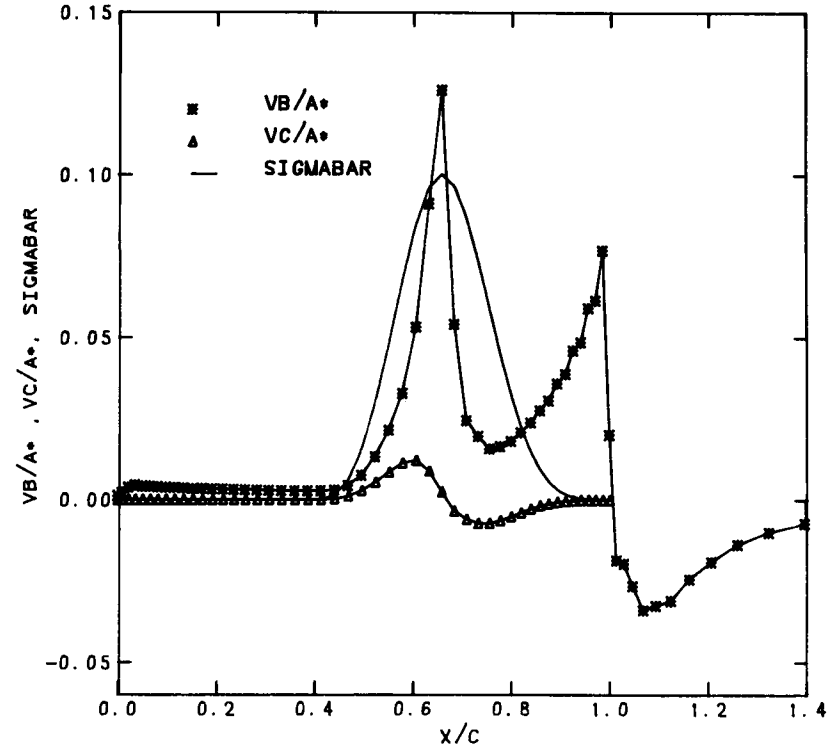

Figure 18. Equivalent and physical mass-weighted transpiration velocities, v_b/a^* and v_c/a^* and the permeability factor $\bar{\sigma}$; upper side of porous RAE 2822 aerofoil

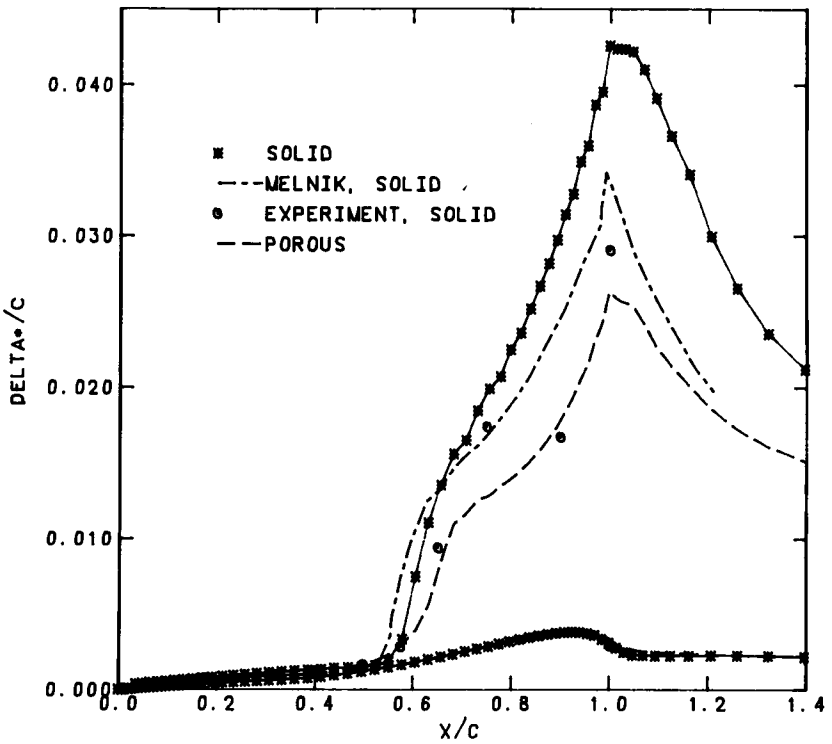

Figure 19. Displacement thickness, δ^*/c; solid and porous RAE 2822 aerofoils

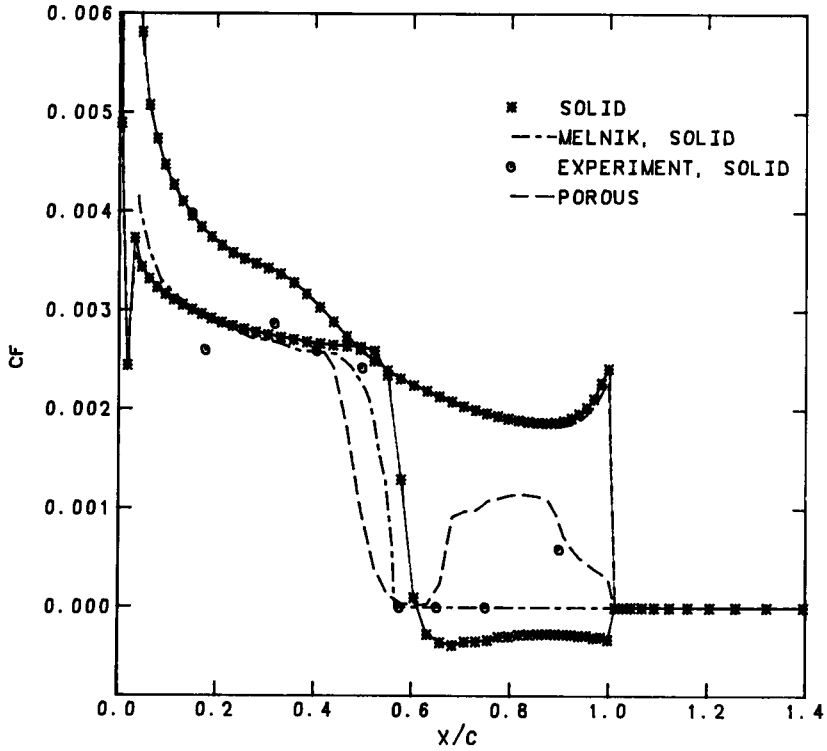

Figure 20. Skin friction coefficient, C_f; solid and porous RAE 2822 aerofoils

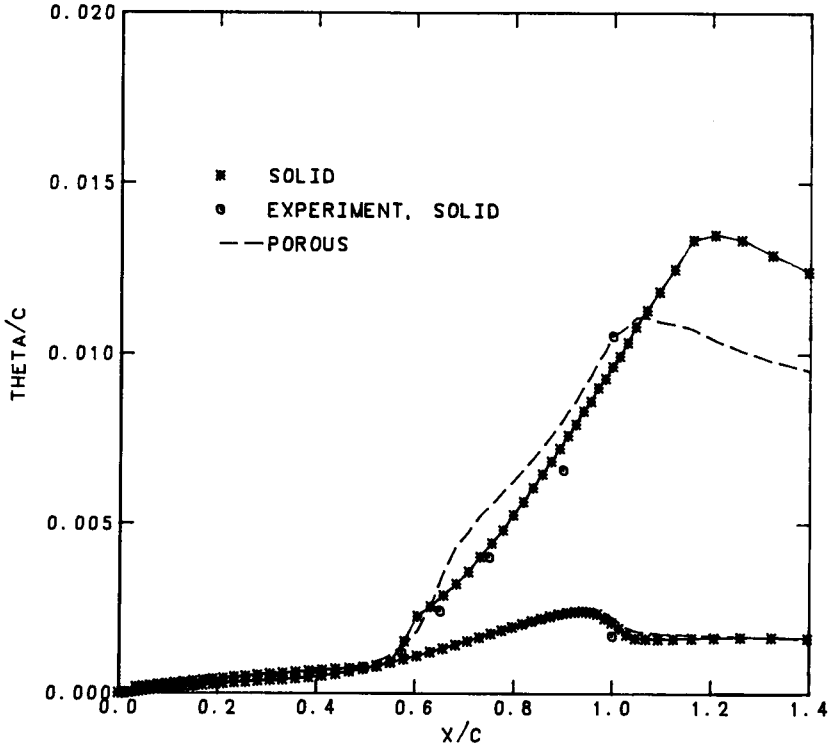

Figure 21. Momentum thickness, θ/c; solid and porous RAE 2822 aerofoils

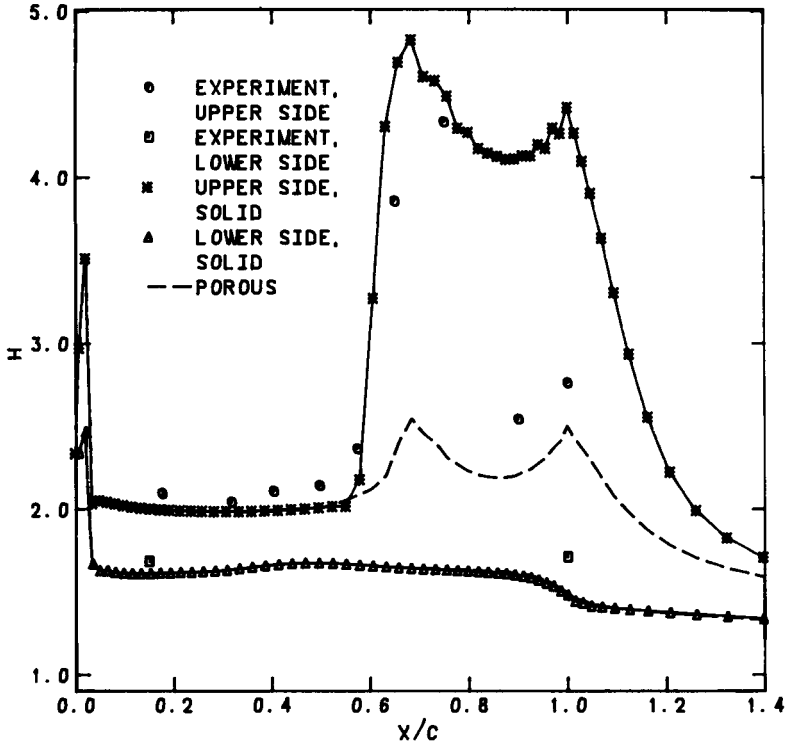

Figure 22. Shape factor, H; solid and porous RAE 2822 aerofoils

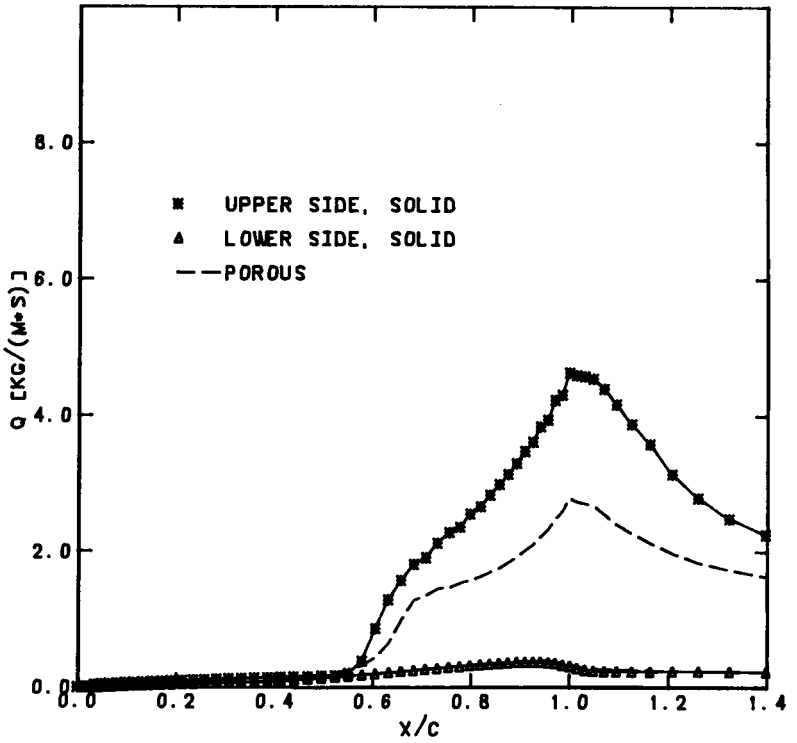

Figure 23. Mass flux defect, Q; solid and porous RAE 2822 aerofoils

CONCLUSIONS

On the basis of the results presented, it can be concluded that coupled viscous–inviscid calculations of transonic separated aerofoil flow, with or without physical transpiration, are feasible. The computations show that passive physical transpiration can lead to a reduced drag coefficient and increased lift coefficient for the permeability factor distributions used in the presented work. The shock strength can be diminished and shock-induced separation can be eliminated. A peaked permeability factor distribution results in smoother solutions than a uniform permeability distribution. If the porosity is too large or the porous region extends too far ahead of the shock, it was observed that the induced blowing ahead of the shock may cause separation there. The aerodynamic performance of aerofoils can be decreased if the porosity is applied in an arbitrary manner, just as the incorrectly applied shock-free design procedure can make shocked aerofoils have even stronger shocks. The shape and size of the cavity under the perforated aerofoil surface has not been analysed. It is expected that it can influence the cavity pressure distribution and, therefore, the aerofoil surface pressure.

Performance of porous aerofoils in an unsteady flow environment represents a real challenge because of the unsteady wave motion inside the cavity underneath the porous aerofoil surface and the possible strong self-induced flow oscillations.

Consequently, it would be highly desirable to approach the entire concept of porous aerofoil design as an inverse problem. Thus, the optimal porosity distribution and its extent should be found so that a minimal possible total aerodynamic drag for the particular aerofoil and given global aerodynamic parameters is obtained.

ACKNOWLEDGEMENT

Both authors are grateful to the Texas Institute for Computational Mechanics (TICOM), The University of Texas at Austin, for providing them with free access to their HARRIS 800 computer. Special thanks are due to reviewers of this paper for their helpful comments and suggestions. This paper is dedicated to the memory of Dr. William McNally of NASA Lewis Research Center.

REFERENCES

1. H. Sobieczky and A. R. Seebass, 'Supercritical airfoil and wing design', *Ann. Rev. Fluid Mech.*, **16,** 337–363 (1984).
2. G. Savu and O. Trifu, 'Porous airfoils in transonic flow', *AIAA J.*, **22,** 989–991 (1984).
3. G. Savu, O. Trifu and L. Z. Dumitrescu, 'Suppression of shocks on transonic airfoils', *14th Int. Symp. on Shock Tubes and Waves*, Sydney, 1983.
4. P. Thiede, P. Krogmann and E. Stanewsky, 'Active and passive shock/boundary-layer interaction control on supercritical airfoils', in *Improvement of Aerodynamic Performance Through Boundary Layer Control and High Lift Systems*, AGARD CP-365, 1984, Paper 24.
5. P. Krogmann, E. Stanewsky and P. Thiede, 'Effects of suction on shock/boundary-layer interaction and shock-induced separation', *J. Aircraft*, **22,** 37–42 (1985).
6. H. T. Nagamatsu, R. V. Ficarra and R. Dyer, 'Supercritical airfoil drag reduction by passive shock wave/boundary layer control in the Mach number range .75 to .90', *AIAA 23rd Aerospace Sciences Meeting*, Reno, Nevada, 14–17 January 1985, AIAA Paper 85-0207.
7. C. R. Olling, 'Viscous–inviscid interaction in transonic separated flow over solid and porous airfoils and cascades', *Ph.D. Dissertation*, Dept. of Aerospace Engineering & Engineering Mechanics, University of Texas at Austin, September 1985.
8. N. Rott and L. F. Crabtree, 'Simplified laminar boundary-layer calculations for bodies of revolution and for yawed wings', *J. Aero. Sci.*, **19,** 553–565 (1952).
9. B. J. Abu-Ghannam and R. Shaw, 'Natural transition of boundary layers—the effects of turbulence, pressure gradient, and flow history', *J. Mech. Eng. Sci.*, **22,** 213–228 (1980).
10. K. Stewartson, 'Correlated incompressible and compressible boundary layers', *Proc. Roy. Soc. (London), Ser. A.*, **200,** 84–100 (1949).

11. J. E. Green, D. J. Weeks and J. W. F. Brooman, 'Prediction of turbulent boundary layers and wakes in compressible flow by a lag-entrainment method', *Aero. Res. Coun., Reports and Memoranda 3791*, 1973.
12. L. F. East, P. D. Smith and P. J. Merryman, 'Prediction of the development of separated turbulent boundary layers by the lag-entrainment method', *R.A.E. TR-77046*, 1977.
13. W. M. Kays and M. E. Crawford, *Convective Heat and Mass Transfer*, 2nd edn, McGraw-Hill, New York, 1980.
14. J. H. Ferziger, *Numerical Methods for Engineering Application*, Wiley, New York, 1981.
15. P. Thiede, G. Dargel and E. Elsholz, 'Viscid–inviscid interaction analysis on airfoils with an inverse boundary layer approach', in E. Haase, (ed.), *Recent Contributions to Fluid Mechanics*, Springer-Verlag, New York, 1982, pp. 244–252.
16. M. R. Collyer, 'An extension to the method of Garabedian and Korn for the calculation of transonic flow past an airfoil to include the effects of a boundary layer and wake', *R.A.E. TP 77104*, 1977.
17. R. C. Lock and M. C. P. Firmin, 'Survey of techniques for estimating viscous effects in external aerodynamics', in P. L. Roe (ed.), *Proceedings of the IMA Conference on Numerical Methods in Aero. Fluid Dynamics, Reading, 1980*, Academic Press, New York, 1982, pp. 337–430.
18. W. R. Van Dalsem, 'Simulation of separated transonic airfoil flow by finite-difference viscous–inviscid interaction', *Ph.D. Dissertation*, Stanford University, 1984.
19. L. B. Wigton, 'Viscous–inviscid interaction in transonic flow', *Ph.D. Thesis*, University of California, Berkeley, 1981.
20. J. E. Carter, 'A new boundary layer inviscid interaction technique for separated flow', *Proc. AIAA 4th Comp. Fluid Dyn. Conf.*, 1979, pp. 45–55.
21. J. C. LeBalleur, 'Strong matching method for computing transonic viscous flows including wakes and separations-lifting airfoils, *La Recherche Aerospatiale* (English edition), No. 1981-3, 1981, pp. 21–45.
22. G. S. Dulikravich and C. R. Olling, 'GSD28-Fortran program for analysis and design of shock-free transonic airfoils and turbomachinery cascades including viscous/inviscid interaction', *Computational Fluid Dynamics Group Research Report 100-85*, Dept. of Aero. Eng. and Eng. Mech., The University of Texas at Austin, September 1985.
23. C.-L. Chen, C.-Y. Chow, T. L. Holst and W. R. Van Dalsem, 'Numerical study of porous airfoils in transonic flow', *NASA TM 86713*, May 1985.
24. J. J. Thibert, M. Grandjacques and L. H. Ohman, 'NACA 0012 airfoil', *Experimental Data Base for Computer Program Assessment*, AGARD Advisory Report No. 138, Paper A1, 1979.
25. J. C. Wai and H. Yoshihara, 'Viscous transonic flow over airfoils', *7th Int. Conf. on Numer. Meth. in Fluid Dynamics*, Stanford University, June 1980; Springer-Verlag, 1981, pp. 417–421.
26. B. M. Giles, 'Newton solution of steady two-dimensional transonic flow', *Thesis*, MIT Dept. of Aero. & Astro., June 1985.
27. M. Drela, 'Two-dimensional transonic aerodynamic design and analysis using the Euler equations', *Thesis*, MIT Dept. of Aero. & Astro., December 1985.
28. C. R. Olling and G. S. Dulikravich, 'Viscous/inviscid computations of transonic separated flows over solid and porous cascades', *ASME paper 86-GT-235, ASME Int. Gas Turbine Conf.*, Dusseldorf, Germany, 8–12, June 1986.
29. G. S. Dulikravich, 'Common misconceptions in the computations of transonic potential flows', *ASME paper 84-GT-211, ASME Int. Gas Turbine Conf.*, Amsterdam, The Netherlands, 3–7, June 1984.
30. Y.-W. Shau, 'Comparative study of numerical dissipation in transonic potential flow calculations', *M.Sc. Thesis*, The University of Texas at Austin, Dept. of Aero. Eng. & Eng. Mech., January 1986.
31. C. R. Olling and G. S. Dulikravich, 'Transonic cascade flow analysis using viscous/inviscid coupling concepts', *AIAA Paper 84-2159, AIAA 2nd Applied Aerodynamics Conf.*, Seattle, WA, 21–23, August 1984.
32. P. H. Cook, M. A. McDonald and M. C. P. Firmin, 'Airfoil RAE 2822—Pressure distributions and boundary layer and wake measurements', *AGARD Advisory Report No. 138*, 1979, Paper A6.
33. R. E. Melnik, H. R. Mead and A. Jameson, 'A multi-grid method for the computation of viscous/inviscid interactions on airfoils', *AIAA Paper 83-0234*, January 1983.